Supporting Information

The role of orientation in the MEL response of OLEDs

Sebastian Engmann[1,2], Emily G. Bittle[2], Lee J. Richter[3], Rawad K. Hallani[4,5], John E. Anthony[4], David J. Gundlach[2]

[1]*Theiss Research, La Jolla, California 92037, United States*

[2]Nanoscale Device Characterization Division, National Institute of Standards and Technology, 101 Bureau Drive, Gaithersburg, Maryland, 20899, United States

[3]Materials Science and Engineering Division, National Institute of Standards and Technology, 101 Bureau Drive, Gaithersburg, Maryland, 20899, United States

[4]Department of Chemistry, University of Kentucky, Lexington, Kentucky, 40506, United States

[5]Current address: KAUST Solar Center, King Abdullah University of Science and Technology, Thuwal 23955-6900, Kingdom of Saudi Arabia

Correspondence and requests for materials should be addressed to D.J.G. (email: david.gundlach@nist.gov) or S.E (email: s.engmann@theissresearch.org)

|	Rubrene	DiF-TES-ADT
HOMO	-5.4 eV	-5.35 eV
LUMO*	-3.2 eV	-3.05 eV
Optical Bandgap	2.23 eV[1, 2]	2.3 eV
CT w/ C60 ($Homo_D$-$Lumo_A$-0.3eV)	1.12 eV	1.07 eV
T_1 (2x T_1)	1.14 eV (2.28 eV)[1-3]	1.08 eV (2.16 eV)[3]
^{1}(TT)	2.1 eV[3]	2.11 eV[3]

Supplementary Table 1 – Molecular and Triplet Levels of Rubrene and DiF-TES-ADT
Molecular and Triplet levels of Rubrene and DiF-TES-ADT. The LUMO values of the materials was estimated from the HOMO level and the optical bandgap, neglecting exciton binding energies.
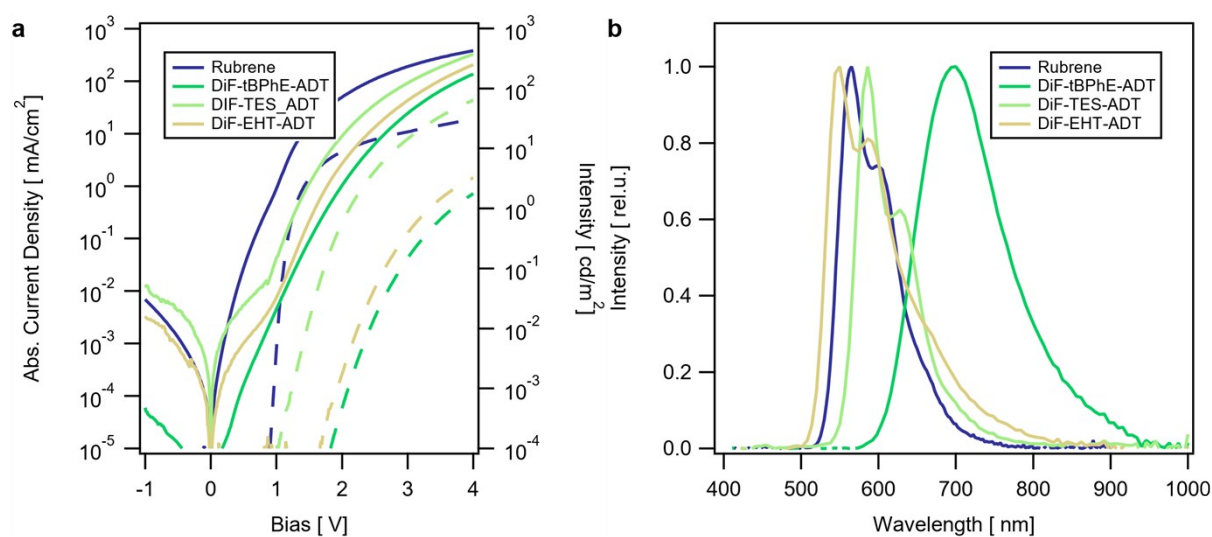
Supplementary Figure 1 - Current Density-Voltage-Luminescence Characteristics
J-V-L-characteristics of devices based on the investigated emitter materials (a). For comparison hetero-junction emission spectra are shown (b).
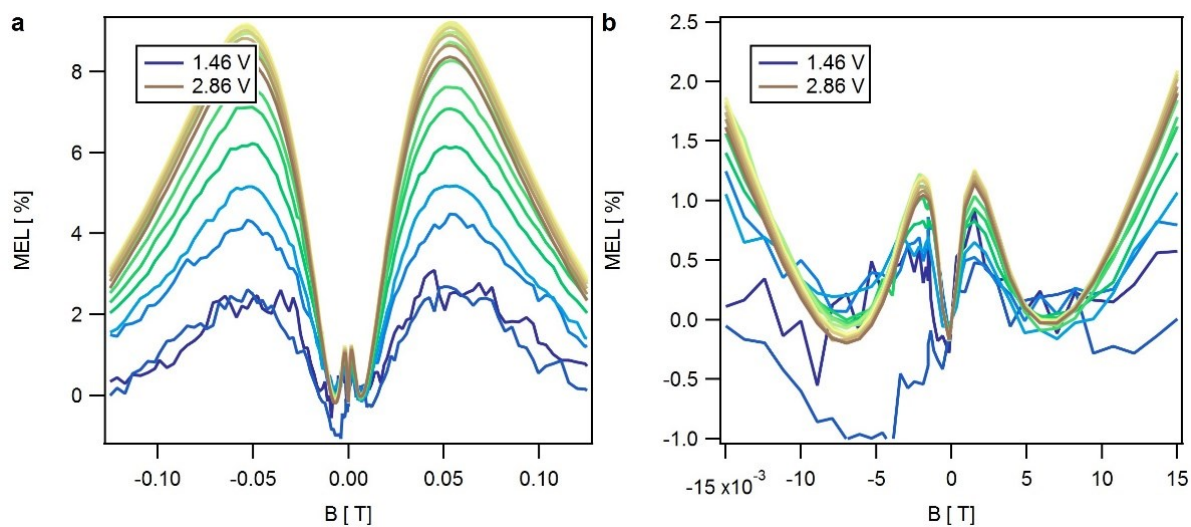

Supplementary Figure 2 - Magneto-electroluminescence Characteristics of DiF-TES-ADT/C$_{60}$ based OLEDs
MEL characteristics for DiF-TES-ADT/C$_{60}$ OLEDs at various applied biases / injection current densities. Shown are the full measured magnetic field range (a) and a zoom-in to small field region (b).

Basic Morphology Investigations

Typically magnetic field effect (MFE) studies either focus on singlet crystal devices and the orientation dependent MFE with respect to an applied external magnetic field, for example transistor measurements of tetracene singlet crystals in OFET devices by Jang et al.[4], or on devices based on spun-coated or evaporated thin films, such as all above mentioned OLED studies. In the thin film devices, crystallinity is typically assumed to be negligible. However, it is known that some small molecules, such as DiF-TES-ADT tend to crystallize. To classify the investigated emitters we took grazing incidence X-ray diffraction (GIXD) data. Shown in **Supplementary Figure 3** are the diffraction patterns for films deposited on silicon substrates with a thin NPD layer to mimic the OLED devices. No diffraction signal was obtained from NPD itself.
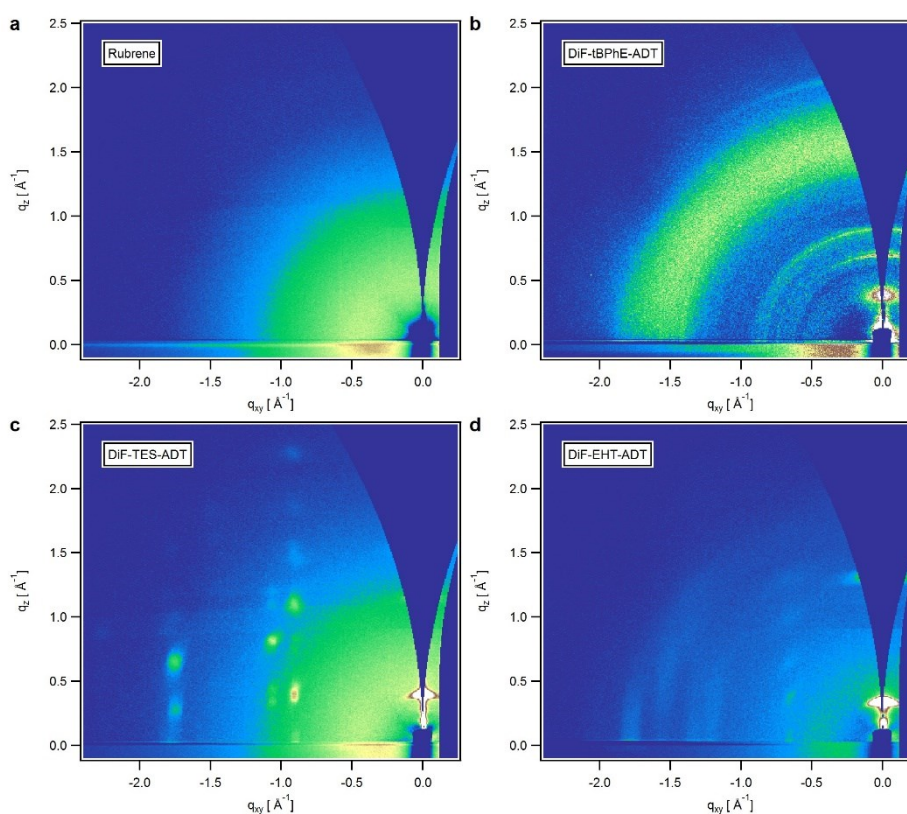

Supplementary Figure 3 - Grazing incidence X-ray diffraction (GIXD)
Grazing incidence X-ray diffraction of a) Rubrene, b) DiF-tBPhE-ADT, c) DiFTES-ADT and d) DiF-EHT-ADT thin films on silicon substrates with NPD.

It is evident that the Rubrene emitter layer is nearly amorphous, as no diffraction features are observable in the corresponding GIXD. In DiF-tBPhE-ADT films one or more peaks of the (00l) series along $q_{xy} \approx 0$ Å^{-1} are present, with an additional feature in DiF-tBPhE-ADT at about 1.56 Å^{-1} - 1.57 Å^{-1}. However the film is still largely isotropic and the measured diffraction patterns it is not possible to address the packing motif. On the other hand, in the

case of DiF-EHT-ADT and DiF-TES-ADT a multitude of diffraction peaks can be observed. Earlier studies have shown that DiF-EHT-ADT crystallizes in a 1D-herringbone motif with a close intermolecular spacing of 3.58 Å and a plane-to-plane distance of 3.56 Å.[5] DiF-TES-ADT crystallizes in a triclinic unit cell[6] with a molecular 2-D π-stacking ("brickwork") motif with high degree of orbital overlap, and strong electronic couplings.[6]
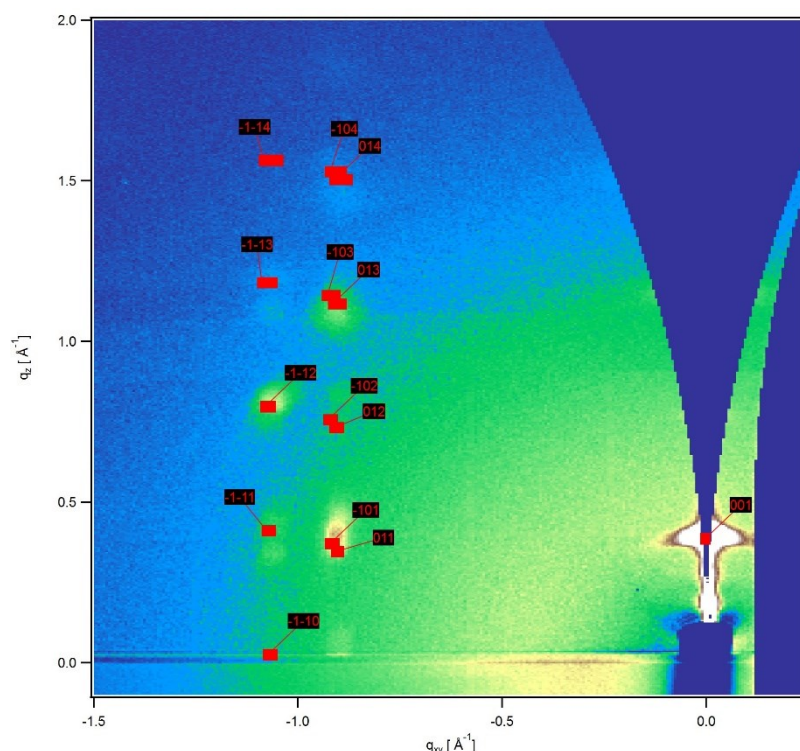

Supplementary Figure 4 - Experimental and Calculated DiF-TES-ADT diffraction pattern
Calculated diffraction pattern for DiF-TES-ADT assuming the single crystal lattice parameters obtained by Paudel et al. [6] : a=7.21Å, b=7.32Å, c=16.35Å, α=87.72°, β=89.99°, γ=71.94°. The calculated pattern corresponds to a average of all azimuthal orientations. The ab-plane is parallel to the sample surface.

In case of the highest ordered film, DiF-TES-ADT, additional tapping-mode atomic force microscopy (AFM) images were taken (**Supplementary Figure 5**) and compared to amorphous Rubrene films. These images show large randomly oriented crystallites supporting the in-plane isotropy. For comparison reasons images of an isotropic Rubrene layer and the surface of the corresponding heterojunctions are shown. The surface of the amorphous Rubrene layer appears very smooth with a root mean square (RMS) value of only 0.82 nm, while the DiF-TES-ADT layer shows large crystallites and a RMS roughness of 21.6 nm. From the AFM images the short axis of the crystallites is determined to be on the scale of 200 nm to 300 nm, and length scales on the order of 500 nm to 700 nm for the long axis. After deposition of a 20 nm C_{60} layer to complete the heterojunction, the surface roughness of the Rubrene based device remains near the emitter only value with RMS = 1.1 nm, the surface roughness of the DiF-TES-ADT based device further increased to RMS = 39.3 nm indicating

4

possibly ongoing crystallization of the donor material during later deposition steps. The large surface roughness of all DiFTES-ADT films effectively leads to a thin intermixed area in all DiFTES-ADT based heterojunction devices and similar effects are expected for other crystalline materials to some extent. Note that this will increase parasitic recombination pathways for charges and excitons within the device, either through increased recombination near the electrodes (homojunctions) and or due to formation of charge transfer states at the emitter:C_{60} interface (heterojunctions). Decreasing parasitic recombination pathways can lead to increased luminescence efficiency and allows for easier observation of TF at medium current densities in these devices, and vice-a-versa an increase in CT-state recombination can lead to reduced luminescence and camouflaged higher order processes.[7]
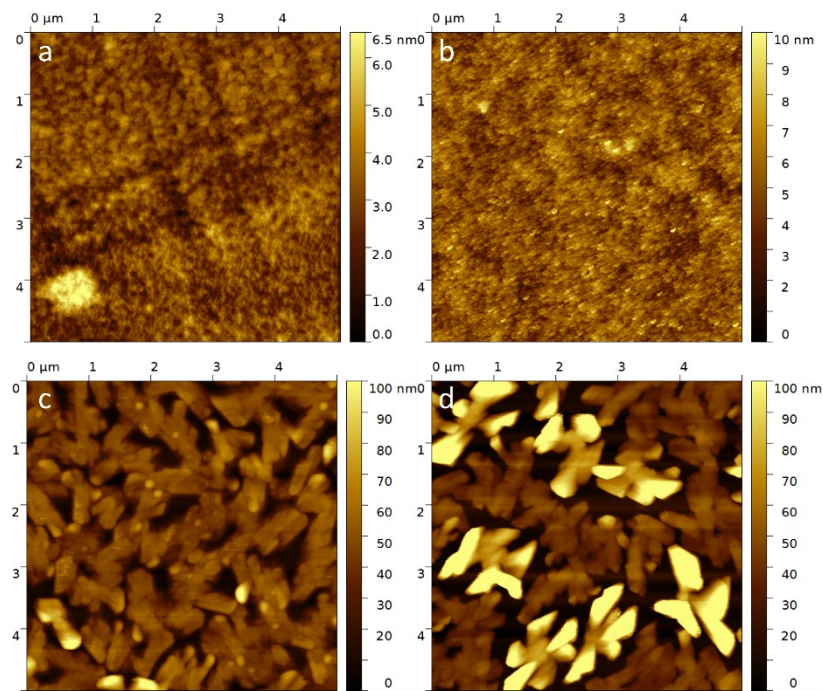
Supplementary Figure 5 – Atomic Force Microscopy images of Rubrene and DiF-TES-ADT films
Atomic Force Microscopy (AFM) images of Rubrene (a) and DiF-TES-ADT (c) films on top of a glass/MoOx(5nm)/NPD(35nm) substrate. Also shown are the surface of the heterojunction after deposition of an additional 20 nm C_{60} on top the emitter layer (b – Rubrene, d – DiF-TES-ADT)

Parameters used for the spin-Hamiltonian

The general form of the spin Hamiltonian is:

$$H = H_{magnetic} + H_{zero-field} + H_{AB} + H_{HFI}$$

where $H_{magnetic} = \mu_B \sum_{i,j} g_{ij} B_i S_j$ describes the Zeeman interaction (μ_B - Bohr magnetron, g-tensor, B - external magnetic field, S - spin operator), $H_{zero-field} = \sum_{i,j} D_{i,j} S_i S_j$ the

intramolecular spin-spin interaction (the *D*-tensor can be expressed in terms of the zero field parameters *D* and *E*), $H_{AB} = \sum_{i,j} J_{ij} S_{A,i} S_{B,j}$ the intermolecular coupling of triplets on molecules A and B and $H_{HFI} = \sum_{i,j} A_{i,j} S_i I_j$ the hyperfine interactions (*A*-hyperfine tensor, *I*-nuclear spin operator).

As described in the main manuscript we do not include hyperfine interactions. To simplify the problem we assume the g-tensor to be isotropic and approximate $g = 2$. The coupling between spins is assumed to be $1.24 \cdot 10^{-2}$ µeV. This leads to a small splitting between all eigenvalues of the spin-Hamiltonian and "true" anti-crossings, see **Supplementary Figure 6**. The zero-field interaction parameter are provided in the manuscript, however we want to clarify that easySpin follows the convention in which the absolute values $D_z > D_y > D_x$ which leads to $0 < E/D < 1/3$. It is important to note that other conventions exists. We refer to the work by Poole et al. who have argued for a standardization of of convention for zero field splitting parameters and provides information about how these numbers can be transformed into different systems.[8]
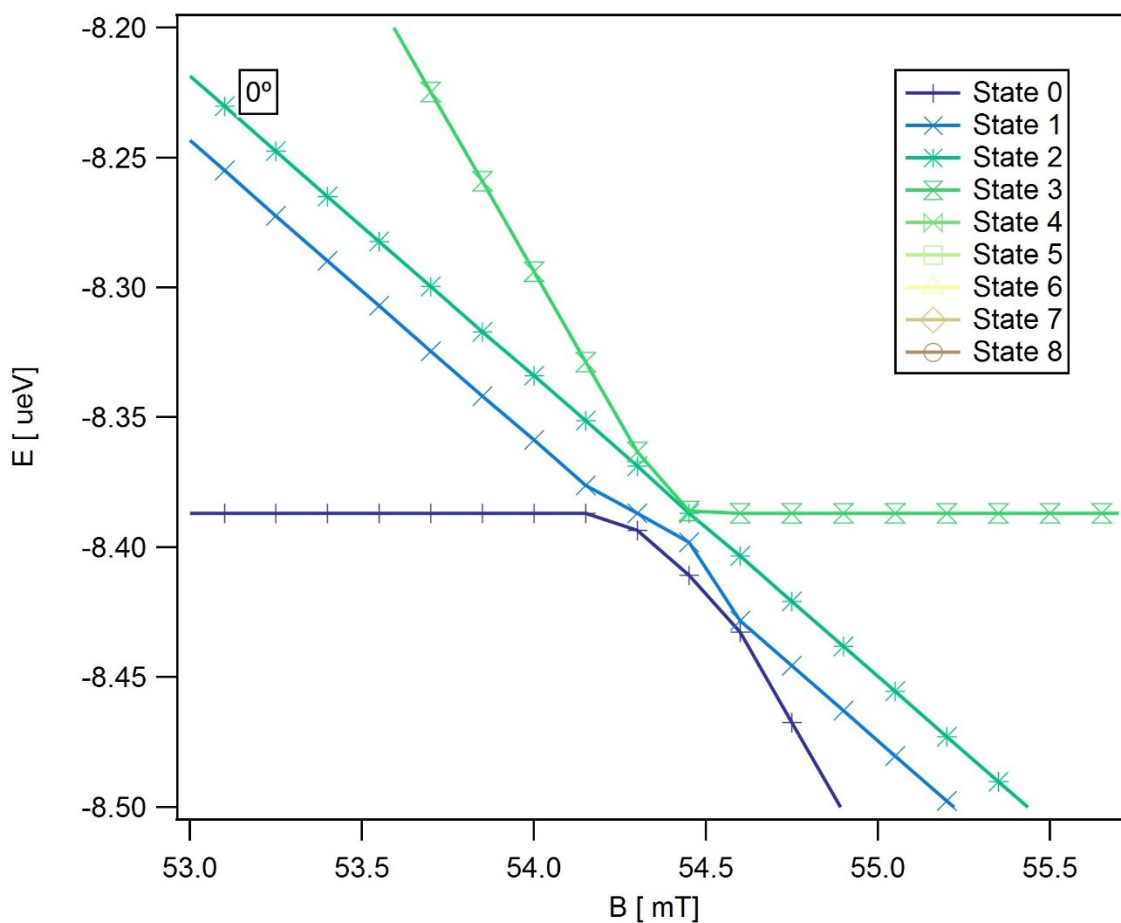
Supplementary Figure 6 – Energy levels
Energy levels for the coherent triplet-pair state in DiF-TES-ADT as function of magnetic field. Shown is a zoomed in region of the 0° graph shown in **Figure 3**a of the main manuscript.

Model - Rate equations:
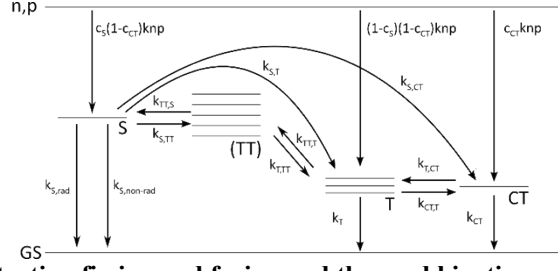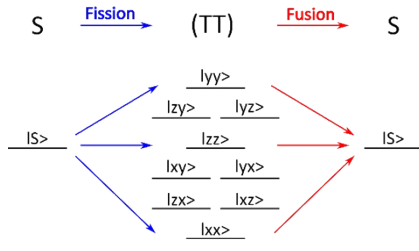
Supplementary Figure 7 - Schematic diagram illustrating fission and fusion and the used kinetic model
Schematic diagram illustrating fission and fusion and the triplet pair states in the zero-field basis. Out of 9 triplet pair states only 3 have singlet character (left). Kinetic model used to calculate the magneto-electroluminescence.

Based on the schematic shown above we derive the following time dependent populations for the CT-state density CT, the uncorrelated triplet state T, the correlated triplet pair ^{3}(TT) and finally singlet state density S:

$$\frac{dnp}{dt} = \frac{J}{q_e a_0} + k_{CT,np}CT - knp$$

$$(5)$$

$$\frac{dCT}{dt} = \left(C_{CT} \cdot knp + k_{S,CT}S + k_{T,CT}T + k_{TT,CT}\sum_{i,j}TT_{i,j} \right) - \left(k_{CT,np} + k_{CT,rec} + k_{CT,TT}T \right)CT$$

$$(6)$$

$$\frac{dT}{dt} = \left((1 - C_S)(1 - C_{CT}) \cdot knp + k_{CT,T}CT + k_{S,T}S + \left(k_{TT,CT} + 2k_{TT,T} \right)\sum_{i,j}TT_{i,j} \right)$$
$$- \left(k_{T,CT} + k_{T,TT}T + k_{T,rec} + k_{CT,TT}CT \right)T$$

$$(7)$$

$$\frac{dTT_{i,j}}{dt} = \left(k_{S,TT}\, C_{s,ij}S + \frac{1}{9} \cdot \frac{1}{2}k_{T,TT}T^2 + \frac{1}{9} \cdot \frac{1}{2}k_{CT,TT}CT \cdot T \right) - \left(k_{TT,CT} + k_{TT,T} + k_{TT,S}C_{S,ij} \right)TT_{ij}$$

$$(8)$$

$$\frac{dS}{dt} = \left(C_s(1 - C_{CT}) \cdot knp + k_{TT,S}\sum_{i,j}C_{S,ij}\,TT_{i,j} \right) - \left(k_{S,rad} + k_{S,nonrad} + k_{S,TT} + k_{S,T} + k_{S,CT} \right)S$$

$$(9)$$

Whereas C_s and C_{CT} are the fractions of free charge carriers that recombine to the singlet and CT state, $C_{S,ij}$ are the magnitude of the wavefunction overlap of the coherent triplet pair and the singlet state as described above. The rates for transitions between the S, TT, T, and CT-states are denoted by k_{mn}, where m corresponds to the initial state and n the final state of the transition. For simplicity we have ignored the generation of a coherent triplet pair from free charges, as this might be expected only at very high current densities / charge carrier densities. We neglected the recombination of the coherent triplet pair to the ground state and allowed only for a decay to 2 triplets, one triplet and a CT-state or conversion to a singlet

state. The equations (5-9) form a system of non-linear equations and can be solved numerically. The MEL response of the device is proportional to:

$$MEL(B,J) = \frac{S(B,J) - S(B=0,J)}{S(B=0,J)}$$

Model – Details on solution of rate equations:

The solution of the spin Hamiltonian will not be discussed. The reader is refereed to the detailed easySpin manual.[9, 10] In the steady state case the solution of the spin Hamiltonian (B-filed dependence) and the kinetic model (leading to the current-dependence) are independent of each other. This might not be the case for rapidly varying B-fields though.

The above system of rate equations was solved numerically for a given set of Cs_{ij} and steady state conditions, e.g. $d/dt = 0$, usigns Matlabs fsolve functionality. The inital guess for the densities S, T, and all of the coherent states TT was made to be proportional to 1/12 of the current density under investigation ($1/12\ J/q_e/a$), e.g. equally distributed states. To ensure positive densities S, T, TT, CT, ... these paramters were feed transformed (square root) into the fsolve alorgithm, and the results squared. The finite differences option used to estimate gradients was "forward". The tolerance was 10^{-6}, essentially forcing the algorithm to run the maximum number of iterations (400 iterations).. The solution for a given current density and B-field was then used as intial guess for the next B-field. The simulations were carried out in a B-field range between -150 mT and 150 mT, with 601 points linearly spaced. In current and field dependent simulations, the B-field dependence was calculated for fixed current density. After each completed MEL(B) calculation the current density was increased and the results of the prior calculation used as intial guess. The current density in these simulations was changed from 0.1 mA/cm^2 to 100 mA/cm^2 with 25 points and exponenial spacing between points.

Model – Extensions:

A word on time-dependent or non-homogenous B-fields, as well as temperature dependent data. Although time dependent data was beyond the scope of this manuscript, as the charm of our approach is the simplicity of DC measurements to investigate basic material properties and spin phenomena, we want to point out that the model can be adapted for this case. Time dependent B-fields, e.g. in form of pulsed microwaves superimposed on an external static field, and or pulsed current device operation will certainly play a role in future spintronic applications. To include time dependence in our basic model, the time evolution of the spin states $|\psi(t)\rangle$ might be considered via time propagation:

$$|\psi(t)\rangle = e^{-iHt/\hbar}|\psi(0)\rangle$$

Additionally, the time aspect of the kinetic model requires the numerical solution of rate equations for $d/dt \neq 0$. In the time dependent case the overall stability of the numerical algorithm might be severely affected by the step size, initial conditions, etc.

To include spatial non-homogenous fields across the sample surface, the model will have to be expanded to lateral dimensions, and new diffusion terms for excitonic states and drift and diffusion terms for charged states might have to be included. If one pursues that route it would be worth extending the method to a 1D-drift-diffussion model first and solve for the exciton and charge distribution within the device thickness (instead of a representative overall

concentration) and homogenous magnetic fields first, and then extend the model from that point to the lateral solution.

Temperature dependence, again beyond the scope of this paper, might be important for future applications too. Here different aspects must be considered separately. First a statistical approach in form of partition function for all the states might be considered. Second the temperature dependence of the spin-Hamiltonian parameters. It is well known within the EPR community and readily understandable that these parameters strongly depend on the molecular arrangement. As the crystal lattice changes upon cooling or heating, e.g. contraction/expansion or possible phase transactions, the spin-Hamiltonian parameters will change, and often not monotonously with temperature. This is not only true for the herein discussed Zero-field terms but also true for hyperfine interaction parameters, etc.

Simulation Parameter - Uniaxial Dif-TES-ADT

J [mA/cm^2]	10
a [cm]	$40 \cdot 10^{-7}$
C_{ct} [rel.u.]	0.5
C_s [rel.u.]	0.25
$k_{CT\text{-}np}$ [s^{-1}]	$1/(50 \cdot 10^{-9})$
$k_{CT,\,recomb}$ [s^{-1}]	$1/(1 \cdot 10^{-12})$
$k_{CT\text{-}T}$ [s^{-1}]	$1/(10 \cdot 10^{-12})$
$k_{CT\text{-}TT}$ [s^{-1}]	0
$k_{T\text{-}recomb}$ [s^{-1}]	$1/(100 \cdot 10^{-6})$
$k_{T\text{-}CT}$ [s^{-1}]	0
$k_{T\text{-}TT}$ [cm^{-3} s^{-1}]	$50 \cdot 10^{-15}$
$k_{TT\text{-}CT}$ [s^{-1}]	0
$k_{TT\text{-}T}$ [s^{-1}]	$1 \cdot 10^{12}$
$k_{TT\text{-}S}$ [s^{-1}]	$10 \cdot 10^{12}$
$k_{non\,Rad}$ [s^{-1}]	$1/(50 \cdot 10^{-12})$
k_{Rad} [s^{-1}]	$1/(15 \cdot 10^{-9})$
$k_{S\text{-}TT}$ [s^{-1}]	$0.1 \cdot 10^{12}$
$k_{S\text{-}T}$ [s^{-1}]	0
$k_{S\text{-}CT}$ [s^{-1}]	$1/(0.2 \cdot 10^{-12})$

Supplementary Table 2 – Simulation Parameter for the Uniaxial DiF-TES-ADT case
Injection current and rate constants used in the simulation of the MEL response for uniaxial DiF-TES-ADT.

The above shown rate constants are on the order of rate constants that others have determined for Rubrene via time delayed fluorescence, time resolved photoluminescence and transient absorption spectroscopy. However, we rounded some numbers and slightly adjusted them. Ryasnyanskiy and Biaggio measured a triplet lifetime τ_T in single Rubrene crystals on the order of 100 μs and a recombination constant k_{TTA} on the order of 10^{-14} cm^3/s.[11] Wen et al.[12], Piland et al.[13], Ma et al. [1, 14], Jankus et al.[15], Tao et al.[16] and others investigated the SF rate and radiative recombination rate in solutions and films. For Rubrene two characteristic lifetimes, τ_{SF}, were determined with the shorter lifetime between 2 ps to 6 ps. The longer lifetime which is delayed due to phonon scattering was determined to be on

the order of 20 ps to 50 ps. Radiative recombination in solution was about 16 ns. We assume a non-radiative lifetime of singlets on the order of the phonon-scattering time (50ps).

It is to note that the magnitude of the constants $k_{\text{TT-T}}$ and $k_{\text{TT-S}}$ is of lesser important in the above model, their ratio though effects the magnitude of the MEL. This is due to the fact that we did not incorporate a recombination channel for the coherent triplet pair that does not lead to singlets or triplets.

Simulation Parameter - Uniaxial Dif-EHT-ADT

Zero-field-splitting parameter: $D = 18$ μeV, $E = 1.2$ μeV

J [mA/cm^2]	10
a [cm]	$40 \cdot 10^{-7}$
C_{ct} [rel.u.]	0.5
C_s [rel.u.]	0.25
$k_{CT\text{-}np}$ [s^{-1}]	$1/(50 \cdot 10^{-9})$
$k_{CT,\,recomb}$ [s^{-1}]	$1/(1 \cdot 10^{-12})$
$k_{CT\text{-}T}$ [s^{-1}]	$1/(10 \cdot 10^{-12})$
$k_{CT\text{-}TT}$ [s^{-1}]	0
$k_{T\text{-}recomb}$ [s^{-1}]	$1/(100 \cdot 10^{-6})$
$k_{T\text{-}CT}$ [s^{-1}]	0
$k_{T\text{-}TT}$ [cm^{-3} s^{-1}]	$5 \cdot 10^{-15}$
$k_{TT\text{-}CT}$ [s^{-1}]	0
$k_{TT\text{-}T}$ [s^{-1}]	$1 \cdot 10^{12}$
$k_{TT\text{-}S}$ [s^{-1}]	$10 \cdot 10^{12}$
$k_{non\,Rad}$ [s^{-1}]	$1/(50 \cdot 10^{-12})$
k_{Rad} [s^{-1}]	$1/(15 \cdot 10^{-9})$
$k_{S\text{-}TT}$ [s^{-1}]	$0.1 \cdot 10^{12}$
$k_{S\text{-}T}$ [s^{-1}]	0
$k_{S\text{-}CT}$ [s^{-1}]	$1/(0.2 \cdot 10^{-12})$

Supplementary Table 3 – Simulation Parameter for the Uniaxial DiF-EHT-ADT case
Injection current and rate constants used in the simulation of the MEL response for uniaxial DiF-EHT-ADT.
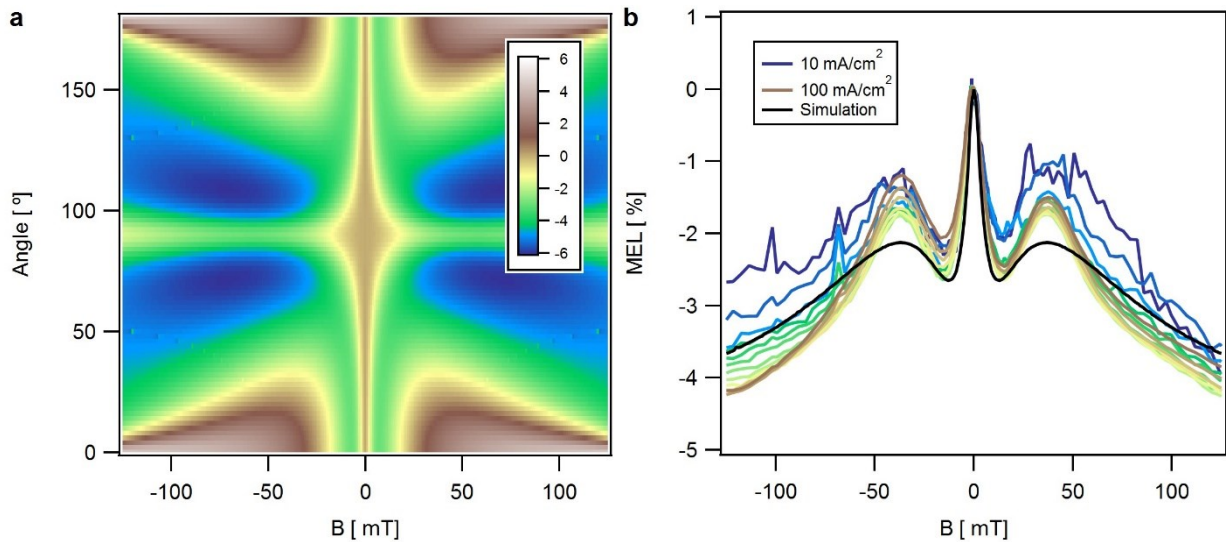

Supplementary Figure 8 - MEL angle dependence and uniaxial average
False color representation of the simulated MEL response as function of azimuth angle and magnetic field (a) and comparison of the calculated uniaxial average (black) and experimental MEL response of DiF-EHT-ADT. Note that the simulation was done at 10mA/cm^2 and we did not reproduce the experimental current dependence.

Model - Amorphous Systems

The case of amorphous systems requires to average the MEL response over all possible spin-orientation to each other and to the external magnetic field. This was discussed on the example of fluorescence measurements of amorphous Rubrene in great detail by Piland et al.[17] and Tapping et al.[18] Shown in **Supplementary Figure 9** is the simulated MEL response of DiF-TES-ADT using the same rates as were used in the simulations above, as well as simulations of Rubrene OLEDs using tetracene literature values for the zero-field splitting parameter D and E of -9.99 μeV and -2.99 μeV, respectively.[18] A summary of the rate constants for the Rubrene case can be found in **Supplementary Table 4**. Note that Piland et al. and Tapping et al. have chosen tetracene to represent Rubrene in their studies but have argued for a wide range of D and E values.[17-19] For this case study the actual values and E/D ratios are of lesser importance as we do not aim to fit the isotropic MEL. We want to note that due to the isotropic averaging D and E values cannot be uniquely determined. However, qualitatively larger D and E values will lead to observation of MEL extrema at larger magnetic fields. In both cases the characteristic "M"-like line-shape that was observed for all the isotropic systems is reasonably reproduced and the additional structure that was observable in the aligned films is lost.
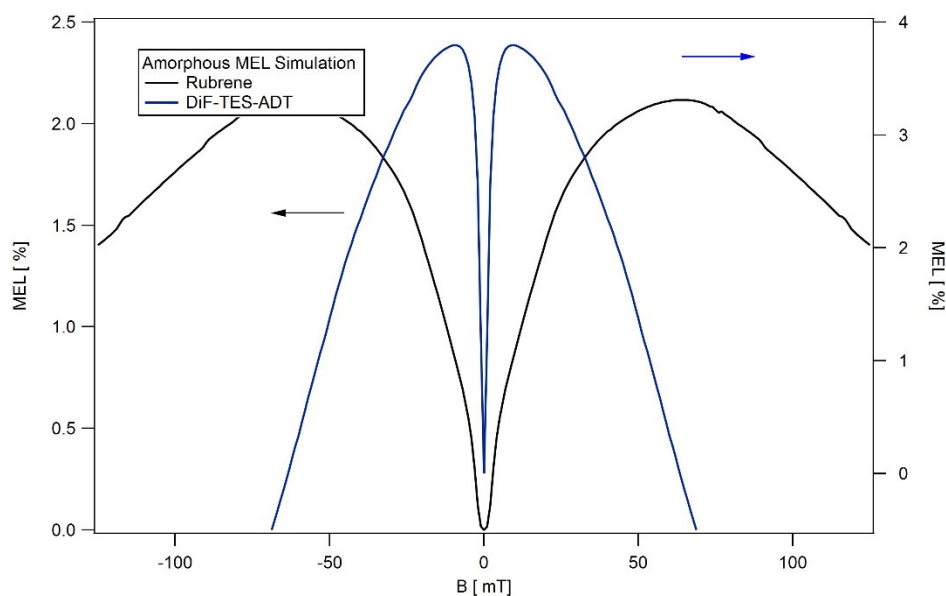

Supplementary Figure 9 - MEL of Amorphous Systems
Simulated MEL response for amorphous DiF-TES-ADT (a) and Rubrene (b) based OLEDs.

12

Model - Poly-crystalline Rubrene:

For completion we have simulated the MEL of crystalline Rubrene devices. Shown in **Supplementary Figure 10** are the angle dependent MEL response for a Rubrene crystal with magnetic field in the ab-plane (a), bc-plabe (b) and ac-plane (c) of the crystal. The averaged MEL response for an poly-crystalline system with symmetry around the sample normal is shown in (d). For comparison (e-h) show the same geometries but in case of DiF-TES-ADT. Also shown in Figure (d) and (h) are the average MEL for crystals that are randomly oriented within the OLED device.
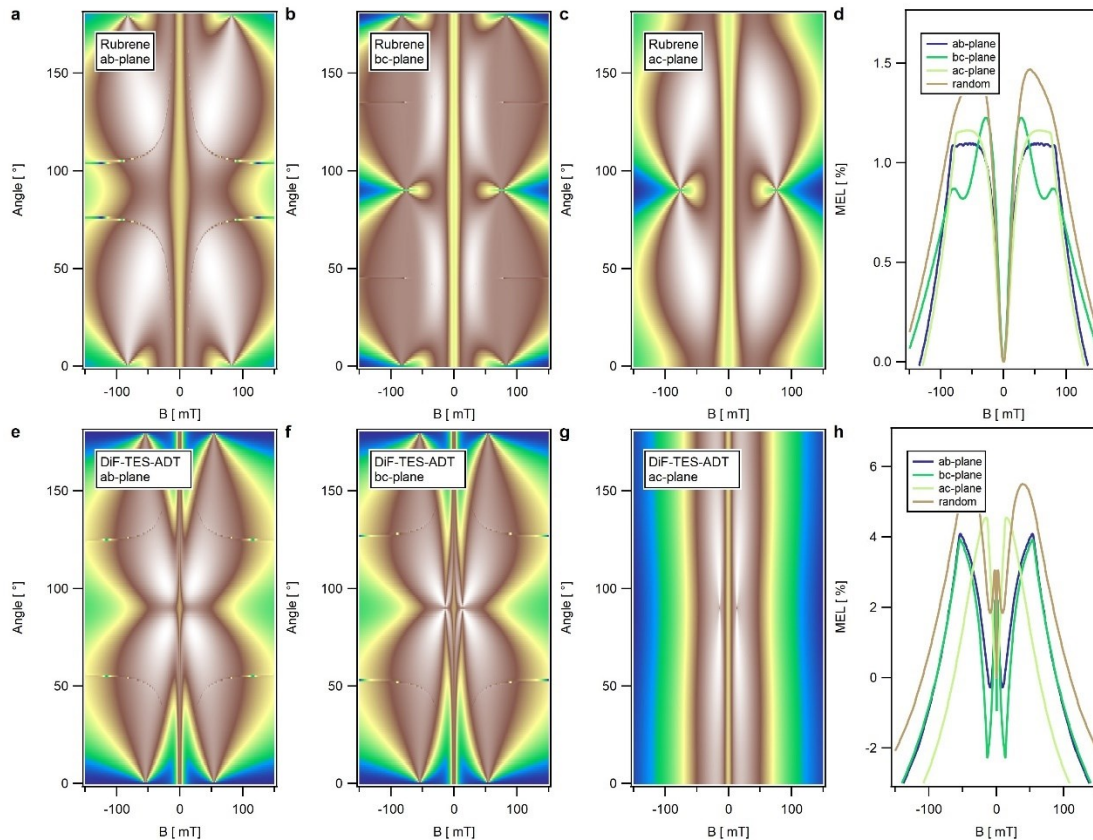
Supplementary Figure 10 - MEL of crystalline Rubrene Systems
Simulated MEL response for crystalline Rubrene devices magnetic field in the (a) ab-plane, (b) bc-plane, (c) ac-plane. Shown in (d) are the uniaxial and isotropic average of rubrene crystallites. Same geometries but for DiF-TES-ADT (e-h).

In all simulated cases a strong angle dependent MEL response with magnetic field in the cyrtsal plane can be observed. Thus, measuring the angle dependent MEL response for crystalline OLEDs would allow the determination of the preferential crystal orientation within the device. However, both materials also differ strongly when one compares the 3 characteristic planes. In case of Rubrene an angle dependence of the magnetic field can be observed for all 3 investigated orientations, while in the case of DiF-TES-ADT only 2 planes show a strong angle dependence and the third is nearly field independent, This can be attributed to the packing of the molecules inside the unit cell relative to the magnetic field and the effect of this arrangement on the corresponding D and E parameter. Rubrene packs in a herringbone motif, assuming that spins follow this symmetry to some extend, it becomes clear that at least one of the spins is never parallel to the magnetic field direction. In the zero-field

parameter this is reflected in a comparably large E (asymmetric component of the D-tensor) *of* -2.9 μeV and E/D ratio of 0.29.

On the other hand, DiF-TES-ADT packs in a brick-wall motif, with parallel molecule backbones. The high alignment of molecules parallel to a crystal plane leads to a small asymmetric component $E = 0.19$ μeV and E/D ratio of 0.03. And a plane in which the spins are nearly parallel to the magnetic field. Interestingly, both materials also strongly differ in the MEL response for randomized samples. While in the Rubrene case a highly structured MEL response can be observed for certain magnetic field orientations, these features get completely averaged out for the case of randomized crystallites, similar to the amorphous case. However, in the DiF-TES-ADT case the characteristic low field maxima remain for a poly-crystalline sample with random crystallites.

Simulation Parameter - Isotropic Rubrene

|	
J [mA/cm^2]	10
a [cm]	$40 \cdot 10^{-7}$
C_{ct} [rel.u.]	0.5
C_s [rel.u.]	0.25
$k_{CT\text{-}np}$ [s^{-1}]	$1/(50 \cdot 10^{-9})$
$k_{CT, recomb}$ [s^{-1}]	$1/(1 \cdot 10^{-12})$
$k_{CT\text{-}T}$ [s^{-1}]	$1/(10 \cdot 10^{-12})$
$k_{CT\text{-}TT}$ [s^{-1}]	0
$k_{T\text{-}recomb}$ [s^{-1}]	$1/(100 \cdot 10^{-6})$
$k_{T\text{-}CT}$ [s^{-1}]	0
$k_{T\text{-}TT}$ [cm^{-3} s^{-1}]	$2.5 \cdot 10^{-15}$
$k_{TT\text{-}CT}$ [s^{-1}]	0
$k_{TT\text{-}T}$ [s^{-1}]	$1 \cdot 10^{12}$
$k_{TT\text{-}S}$ [s^{-1}]	$10 \cdot 10^{12}$
$k_{non Rad}$ [s^{-1}]	$1/(50 \cdot 10^{-12})$
k_{Rad} [s^{-1}]	$1/(15 \cdot 10^{-9})$
$k_{S\text{-}TT}$ [s^{-1}]	$0.1 \cdot 10^{12}$
$k_{S\text{-}T}$ [s^{-1}]	0
$k_{S\text{-}CT}$ [s^{-1}]	$1/(0.2 \cdot 10^{-12})$

Supplementary Table 4 – Simulation Parameter for the isotropic Rubrene case
Injection current and rate constants used in the simulation of the MEL response for isotropic Rubrene.

Simulation Parameter - Current Dependent MEL response

$J\ [\text{mA/cm}^2]$	0.1 - 100
$a\ [\text{cm}]$	$40 \cdot 10^{-7}$
$C_{ct}\ [\text{rel.u.}]$	0.5
$C_s\ [\text{rel.u.}]$	0.25
$k_{CT\text{-}np}\ [\text{s}^{-1}]$	$1/(50 \cdot 10^{-9})$
$k_{CT,\,recomb}\ [\text{s}^{-1}]$	$1/(1 \cdot 10^{-12})$
$k_{CT\text{-}T}\ [\text{s}^{-1}]$	$1/(10 \cdot 10^{-12})$
$k_{CT\text{-}TT}\ [\text{s}^{-1}]$	0
$k_{T\text{-}recomb}\ [\text{s}^{-1}]$	$1/(100 \cdot 10^{-6})$
$k_{T\text{-}CT}\ [\text{s}^{-1}]$	0
$k_{T\text{-}TT}\ [\text{cm}^{-3}\ \text{s}^{-1}]$	see **Table 1**
$k_{TT\text{-}CT}\ [\text{s}^{-1}]$	0
$k_{TT\text{-}T}\ [\text{s}^{-1}]$	$1 \cdot 10^{12}$
$k_{TT\text{-}S}\ [\text{s}^{-1}]$	$10 \cdot 10^{12}$
$k_{non\,Rad}\ [\text{s}^{-1}]$	$1/(50 \cdot 10^{-12})$
$k_{Rad}\ [\text{s}^{-1}]$	$1/(15 \cdot 10^{-9})$
$k_{S\text{-}TT}\ [\text{s}^{-1}]$	see **Table 1**
$k_{S\text{-}T}\ [\text{s}^{-1}]$	0
$k_{S\text{-}CT}\ [\text{s}^{-1}]$	$1/(0.2 \cdot 10^{-12})$

Supplementary Table 5 – Shared Simulation Parameter for the currend dependent MEL
Injection current and rate constants used in the simulation of the current dependent MEL response.
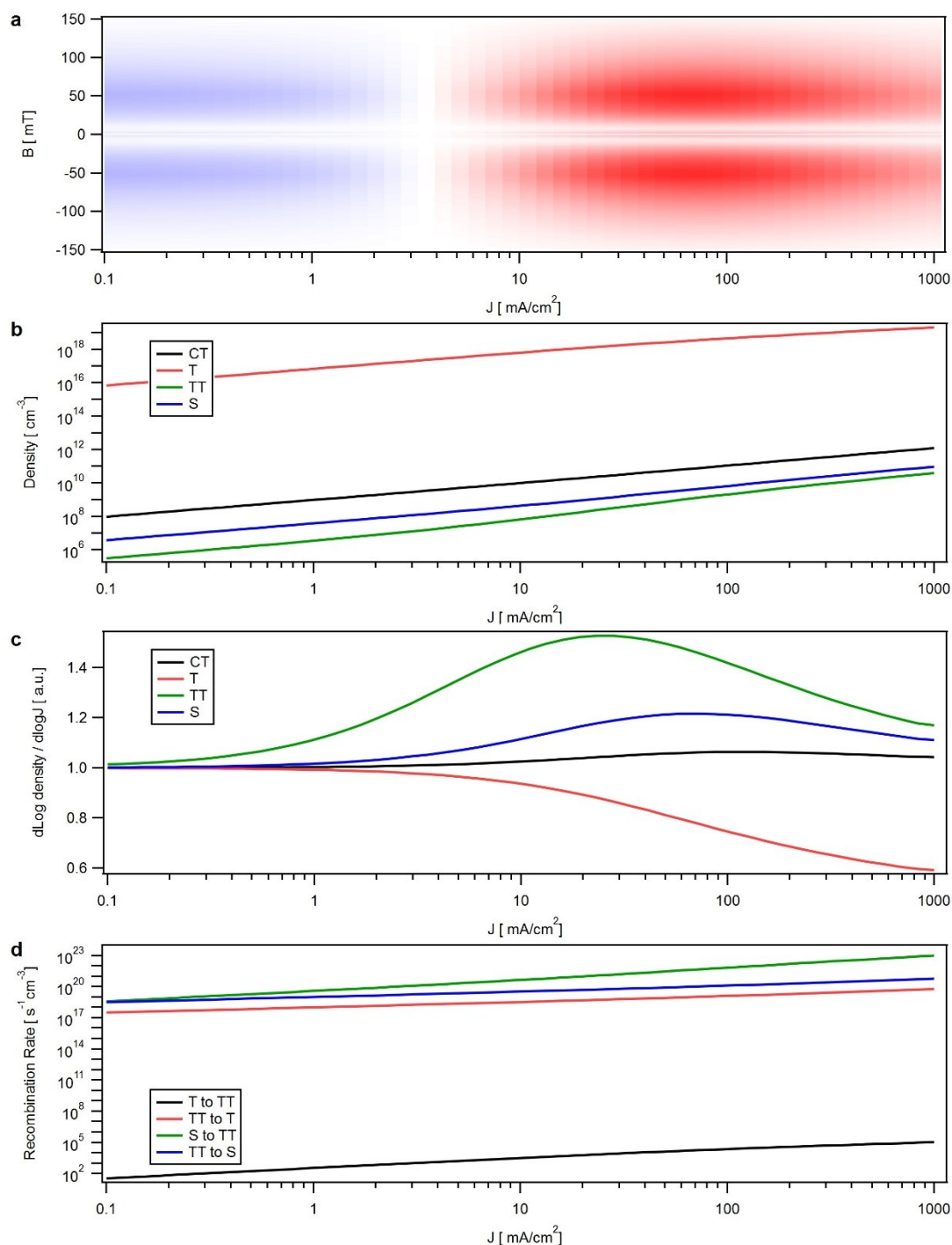
Supplementary Figure 11 - MEL and derived Population densities

Simulated MEL response for the same parameter as Shown in Figure 6c), but over a wider current density range. Shown in a) is the MEL response, b) shows the calculated population density of CT, T, the sum of all TT and S states. c) shows the exponent in the dependencies of density $\sim J^n$. Shown in d) are the recombination rates for the transitions S to TT and T to TT and vice a versa.

References

1.   Ma, L., et al., *Singlet fission in rubrene single crystal: direct observation by femtosecond pump-probe spectroscopy.* Physical Chemistry Chemical Physics, 2012. **14**(23): p. 8307-8312.

2.   Miyata, K., et al., *Coherent singlet fission activated by symmetry breaking.* Nature Chemistry, 2017. **9**: p. 983.

3.   Yong, C.K., et al., *The entangled triplet pair state in acene and heteroacene materials.* Nature Communications, 2017. **8**: p. 15953.

4.   Jang, H.-J., et al., *Electrical Detection of Singlet Fission in Single Crystal Tetracene Transistors.* ACS Nano, 2019. **13**(1): p. 616-623.

5.   Hallani, R.K., *Designing Anthradithiophene Derivatives Suitable For Applications in Organic Electronics and Optoelectronics*, in *Chemistry*. 2015, University of Kentucky: https://uknowledge.uky.edu/chemistry_etds/61.

6.   Ward, J.W., et al., *Tailored interfaces for self-patterning organic thin-film transistors.* Journal of Materials Chemistry, 2012. **22**(36): p. 19047-19053.

7.   Engmann, S., et al., *Higher order effects in organic LEDs with sub-bandgap turn-on.* Nature Communications, 2019. **10**(1): p. 227.

8.   Poole, C.P., H.A. Farach, and W.K. Jackson, *Standardization of convention for zero field splitting parameters.* The Journal of Chemical Physics, 1974. **61**(6): p. 2220-2221.

9.   Stoll, S. and A. Schweiger, *EasySpin, a comprehensive software package for spectral simulation and analysis in EPR.* Journal of Magnetic Resonance, 2006. **178**(1): p. 42-55.

10.   2021 [cited 2021; Available from: https://easyspin.org/easyspin/documentation/.

11.   Ryasnyanskiy, A. and I. Biaggio, *Triplet exciton dynamics in rubrene single crystals.* Physical Review B, 2011. **84**(19): p. 193203.

12.   Wurfel, P., *The chemical potential of radiation.* Journal of Physics C: Solid State Physics, 1982. **15**(18): p. 3967.

13.   Nie, H., et al., *Modulation of Aggregation-Induced Emission and Electroluminescence of Silole Derivatives by a Covalent Bonding Pattern.* Chemistry – A European Journal, 2015. **21**(22): p. 8137-8147.

14.   Lee, T.W., et al., *Self-Organized Gradient Hole Injection to Improve the Performance of Polymer Electroluminescent Devices.* Advanced Functional Materials, 2007. **17**(3): p. 390-396.

15.   Lee, T.-W., et al., *Hole-injecting conducting-polymer compositions for highly efficient and stable organic light-emitting diodes.* Applied Physics Letters, 2005. **87**(23): p. 231106.

16.   Wetzelaer, G.A.H., et al., *Origin of the dark-current ideality factor in polymer:fullerene bulk heterojunction solar cells.* Applied Physics Letters, 2011. **99**(15): p. 153506.

17.   Piland, G.B., et al., *Magnetic Field Effects on Singlet Fission and Fluorescence Decay Dynamics in Amorphous Rubrene.* The Journal of Physical Chemistry C, 2013. **117**(3): p. 1224-1236.

18.   Tapping, P.C. and D.M. Huang, *Comment on "Magnetic Field Effects on Singlet Fission and Fluorescence Decay Dynamics in Amorphous Rubrene".* The Journal of Physical Chemistry C, 2016. **120**(43): p. 25151-25157.

19.   Piland, G.B. and C.J. Bardeen, *Reply to "Comment on 'Magnetic Field Effects on Singlet Fission and Fluorescence Decay Dynamics in Amorphous Rubrene'".* The Journal of Physical Chemistry C, 2016. **120**(43): p. 25158-25160.